

0.1

Introduction

The study of chaotic dynamics has been an active area of interdisciplinary research since the 1970s. Today, researchers are interested in practical applications of chaos, such as communications [1, 2], ranging [3] and ultra-wide-band (UWB) sensor networks [4], which require simple devices that produce complex and high-speed dynamics. To produce the high-dimensional chaos required for applications, a nonlinear system needs to have a high-dimensional phase space. One way to achieve this effect in relatively simple devices is to incorporate time-delayed feedback, as depicted in Fig. 1. Furthermore, since all physical signals travel at finite speeds, it is important to understand how inherent time delays in both natural and man-made systems interact with nonlinearities to influence their behavior.

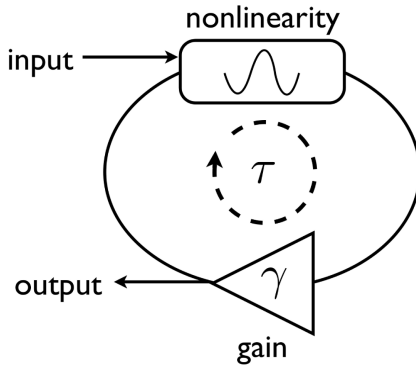


Figure 1 Schematic of a simple nonlinear time-delay system with feedback gain γ and time delay τ .

Time-delayed feedback systems obey delay differential equations (DDEs), rather than ordinary differential equations (ODEs). A DDE is an equation in which the state of a dynamic variable at a given time depends on the values of the dynamic variables at both current and previous times, unlike ODEs where only values at current times matter [5]. An example of a generic DDE with a single time delay τ is given by

$$\dot{x}(t) = F[x(t), x(t - \tau)], \tag{1}$$

where F is an arbitrary function of the current and delayed variables.

The phase space corresponding to a DDE is infinite-dimensional, allowing for the possibility of the previously mentioned high-dimensional chaotic solutions. Therefore, systems with sufficiently long time-delayed feedback can often be comprised of a small number of simple components and yet can still give rise to rich dynamics (including chaos) due to their infinite-dimensional phase space.

Studying experimental time-delayed feedback systems has provided much-needed insight about the solutions and properties of particular classes of DDEs. Since DDEs are commonly used to model the behavior of many types of systems (*i.e.*, physiological diseases [6], population dynamics [7], neuronal networks [8], as well as nonlinear optical devices [9]), these results have important implications for many different fields of study.

One example of such a result is the broadband chaos we observe in a particular nonlinear time-delayed feedback system: an optoelectronic oscillator. The spectra of typical chaotic devices are broadband, yet they often contain several sharp peaks that stand out above the broad background. These features correspond to weakly unstable periodic orbits that comprise the backbone of the strange attractor. The fact that the power spectra for typical chaotic devices are not featureless limits their utility in the applications mentioned above.

In contrast, we will show in this Chapter that our optoelectronic oscillator displays high-speed chaos with an essentially featureless power spectrum for certain choices of parameter values, as reported in Ref. [10]. The flat nature of the spectrum makes it difficult to distinguish from white noise, which could be attractive for use in applications where one wants there to be a low probability of detecting the deterministic signal.

Additionally, we find that the chaotic behavior coexists with a linearly-stable quiescent state. If the system starts in this state, a finite perturbation of sufficient amplitude can force the system to the chaotic state. Furthermore, the transition between the two states takes the form of a train of ultrafast pulses that overlap and merge to eventually give rise to the chaotic solution. We will explain how these observations motivate a nonlinear stability analysis of the steady-state, which yields excellent agreement with our experimental results.

0.2 Optoelectronic oscillators

Optoelectronic oscillators have frequently been used as a bench-top tool for studying nonlinear time-delayed feedback, with their origins dating back to the seminal work of Ikeda [9]. The essential ingredients for such a system include: a constant intensity optical power source, a nonlinear device to modulate the optical signal, an element to provide gain to compensate for any losses, and a feedback delay line with a timescale longer than the characteristic timescales of the resulting dynamics. The finite propagation time necessary for light to traverse the loop and its nonlinear interaction with the modulator results in new types of instabilities. In particular, Ikeda showed that multiple stable steady-states and periodic states can coexist for the same parameter values. Ikeda also showed numerically that, as the feedback gain is slowly increased, the steady-state becomes unstable and subsequently undergoes a period-doubling bifurcation to chaos. Shortly after Ikeda's prediction in 1979, this behavior was first observed experimentally by Gibbs *et al.* [11] in 1981.

After the pioneering work of Ikeda and others, several more experiments were

designed in order to investigate the behavior of nonlinear time-delayed feedback systems. One reason these devices became so popular is that the generated chaos could be of arbitrarily high dimension: Farmer showed that the dimension of chaotic attractor increases as a function of the delay [12]. Additionally, the speed of these systems began to increase with advances in technology, making them even more attractive for certain applications. Along with the increase in speed, however, came components that were ac-coupled, meaning that signals below a certain frequency (f_h) were blocked. This led to a new class of DDEs, which is used to model modern high-speed optoelectronic oscillators.

The dynamics of this new class of high-speed optoelectronic oscillator were recently studied by Peil *et al.* [13]. They showed both experimentally and numerically that their device was capable of producing a variety of rich behaviors, including: fast square-wave solutions, low-frequency periodic solutions, breathers [14], multipulse dynamics, and chaos. In addition to its wide range of dynamics, the utility of this device has also been successfully demonstrated in the realm of secure chaos communication [15]. The chaos generated by the optoelectronic oscillator was used to encode a message, and the resulting signal was transmitted over 120 km of optical fiber using the metropolitan area network of Athens, Greece. The message was then retrieved using chaos synchronization with an identical device at the end of the line. The transmission rates were on the order of gigabits per second.

Our optoelectronic oscillator is similar to the one studied in Ref. [13]. In greater detail, and as shown in Fig. 2, the beam generated by a continuous-wave semiconductor laser (wavelength $1.55 \mu\text{m}$) is injected into a single-mode optical fiber, passes through a polarization controller and optical attenuator, and is injected into a Mach-Zehnder modulator (MZM). Light exiting the modulator passes through an additional piece of single-mode fiber (length ~ 5 m) serving as a delay line and is incident on a photodetector. Half of the resulting signal, denoted by V , is amplified by an inverting modulator driver (gain $g_{\text{MD}} = -22.6$) and fed back to the MZM via the ac-coupled input port. The other half of the signal is directed to a high-speed oscilloscope (8 GHz analog bandwidth, 40 GS/s sampling rate). The gain in the feedback loop, the bias voltage applied to the MZM, and the length of the time delay are all easily accessible parameters that determine the dynamics of the measured voltage.

To model the dynamics of the optoelectronic system one needs to consider: the nonlinear transmission functions of the MZM and modulator driver, the finite bandwidth of the system components, and the amount of time it takes the signal to propagate from the output of the MZM back to the radio frequency (rf) input of the MZM.

The MZM modulates the intensity of an incident optical signal by exploiting Pockels electro-optic effect in a lithium niobate crystal in one arm of a Mach-Zehnder interferometer. When the signals from each arm of the interferometer are recombined at the output, their resulting interference depends on a constant bias voltage (V_B) and a fluctuating rf voltage ($V_{\text{in}}(t)$) applied to two electrodes across the crystal. The optical power (P_{out}) transmitted through the devices is given by

$$P_{\text{out}} = P_{\text{in}} \cos^2 \left[\frac{\pi}{2} \left(\frac{V_B}{V_{\pi,\text{dc}}} + \frac{V_{\text{in}}}{V_{\pi,\text{rf}}} \right) \right], \quad (2)$$

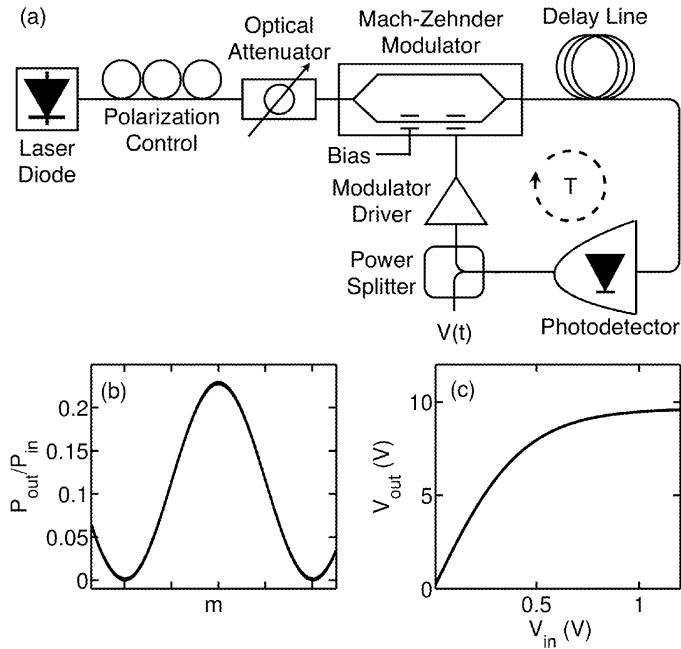


Figure 2 (a) Schematic of optoelectronic oscillator. Nonlinear transmission functions of MZM (b) and modulator driver (c).

where P_{in} is the power incident on the MZM, and $V_{\pi,dc}$ and $V_{\pi,rf}$ characterize the widths of the interference fringe ($V_{\pi,rf}=7.4$ V, $V_{\pi,dc}=7.7$ V). The interference fringe obtained by slowly varying V_B is shown in Fig. 2b.

The modulator driver also has a nonlinear response: it saturates at high voltage with a saturation voltage of $V_{sat} = 9.7$ V. We model this saturation with a hyperbolic tangent function, as shown in Fig. 2c. We find it essential to take into account this additional nonlinearity, as it limits the extent to which we can access multiple fringes of the MZM interference curve.

The high-speed components in our device are bandpass-coupled so that feedback of both low and high frequencies are suppressed. This differs from Ikeda's original model, which only incorporated low-pass filtering, and it has been shown that the inclusion of a high-pass filter results in fundamentally different dynamics [16]. We use a two-pole bandpass filter to approximate the effects of bandpass coupling, with low- (high-) frequency cut-off $\omega_- = 1.5 \times 10^5$ s $^{-1}$ ($\omega_+ = 7.5 \times 10^{10}$ s $^{-1}$), center frequency $\omega_0 = \sqrt{\omega_- \omega_+} = 1.1 \times 10^8$ s $^{-1}$, and bandwidth $\Delta = \omega_+ - \omega_- = 7.5 \times 10^{10}$ s $^{-1}$.

Finally, we measure the time delay of the feedback loop to be approximately 24 ns. Thus, our oscillator has three widely separated timescales: the time delay of the

feedback (on the order of ten nanoseconds), the high-pass filter response time (on the order of microseconds), and the low-pass filter response time (on the order of ten picoseconds). Other researchers have found that these timescales play a prominent role in the dynamics they observe [13].

By combining the effects of the nonlinearities, bandpass filtering and time delay, we derive an integro-delay differential equation describing the fluctuating voltage $V(t)$ [17]

$$V(t) + \frac{1}{\Delta} \frac{dV(t)}{dt} + \frac{\omega_0^2}{\Delta} \int_0^t V(l) dl = G \cos^2 \left\{ \frac{\pi V_B}{2V_{\pi,dc}} + \frac{\pi V_{sat}}{2V_{\pi,rf}} \tanh \left[\frac{g_{MD} V(t-T)}{V_{sat}} \right] \right\}, \quad (3)$$

where G characterizes the gain in the feedback loop (proportional to the injected optical power) in units of Volts and all other variables have previously been defined. We can then rewrite this integro-delay differential equation as two coupled DDEs given by

$$\frac{1}{\Delta} \frac{dV(t)}{dt} = -V(t) - U(t) + G \cos^2 \left\{ m + d \tanh \left[\frac{g_{MD} V(t-T)}{V_{sat}} \right] \right\}, \quad (4)$$

$$\frac{1}{\Delta} \frac{dU(t)}{dt} = \frac{\omega_0^2}{\Delta^2} V(t), \quad (5)$$

where $m = \pi V_B / 2V_{\pi,rf}$ is the dimensionless operating point of the nonlinearity and $d = \pi V_{sat} / 2V_{\pi,rf}$ characterizes the saturation of the modulator driver. By defining dimensionless variables

$$x = \frac{g_{MD}}{V_{sat}} V, \quad (6)$$

$$y = \frac{g_{MD}}{V_{sat}} U - \gamma \cos^2 m, \quad (7)$$

and rescaling time ($s = t\Delta$), we obtain two coupled dimensionless DDEs

$$\dot{x}(s) = -x(s) - y(s) + F[x(s-\tau)], \quad (8)$$

$$\dot{y}(s) = \epsilon x(s). \quad (9)$$

Here, the overdot denotes the derivative with respect to the dimensionless time s , γ is the dimensionless feedback loop gain, $\tau = T\Delta$ is the dimensionless time delay, $\epsilon = \omega_0^2 / \Delta^2$ characterizes the bandpass filter, and the nonlinear delayed feedback term is

$$F[x] = \gamma \cos^2 (m + d \tanh x) - \gamma \cos^2 m. \quad (10)$$

In our experiments, three parameters are held fixed ($d=2.1$, $\tau=1820$, and $\epsilon=2.0 \times 10^{-6}$), while γ can range from 0 – 5 by adjusting the injected optical power with an attenuator and m ranges from $-\pi/2$ to $\pi/2$. For future reference, note that V and its dimensionless analog x have opposite signs because $g_{MD} < 0$.

6 |

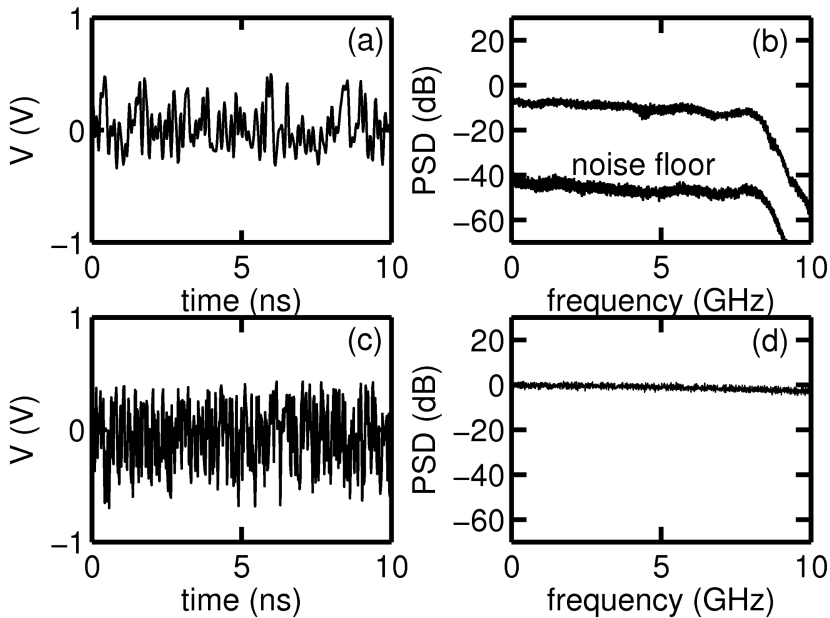


Figure 3 The experimental time series (a) and power spectral density (b) of the broadband chaotic behavior in the optoelectronic oscillator for $m = 0.063$ and $\gamma = 3.47$ (upper trace). We find that the spectrum is flattest (i.e. the small peaks corresponding to T nearly vanish) for $m \gtrsim 0$. The power spectral density of the noise floor obtained below threshold (lower trace) is also shown. Theoretically predicted time series (c) and power spectral density (d) for $m = 0.063$ and $\gamma = 3.47$. The numerical time series contains higher frequency components than the experimental time series, since the bandwidth of the oscilloscope affects the experimental time series.

One important distinction of our work is that we bias the MZM near the top of an interference fringe ($m \approx 0$), which, as we will show in the next section, is where the quiescent state of the system is the most linearly-stable. It is in this regime where we obtain the broadband chaotic behavior shown in Fig. 3a. The one-sided power spectral density (PSD) of the experimental chaotic time series with a resolution bandwidth of 8 MHz is shown in Fig. 3b. One can see that the power spectrum is essentially ‘featureless,’ as it is roughly flat up to the cutoff frequency of the oscilloscope used to measure the dynamics (8 GHz). More precisely, the spectrum is contained within a range of 12 dB with a standard deviation of 2 dB for frequencies below 8 GHz.

To further emphasize the flatness of the chaotic spectrum, we compare our results to the case where the oscillator is in the quiescent state, just below the instability threshold to be discussed in the next section. As seen in Fig. 3b, the PSD is at least 40 dB below the PSD of the chaotic state and is qualitatively consistent with the noise-floor of the overall system. Quantitatively, the noise floor is contained within

a range of 18 dB with a standard deviation of 2 dB. Comparing the statistics for both spectra shows that the spectrum of the broadband chaos is nearly as featureless as the spectrum of the system noise.

One can obtain a qualitatively similar time series and spectrum by integrating the (noise-free) Eqs. 8 and 9, as shown in Figs. 3c and 3d, indicating that the flat, broad spectrum is due to the deterministic dynamics rather than experimental noise. We also determine a positive largest Lyapunov exponent of $\sim 0.03 \text{ ns}^{-1}$, showing that the trajectory is indeed chaotic.

In the following sections we will explain how this broadband chaotic solution can be accessed with either experimental noise or a controlled perturbation, despite the fact that we are operating in the regime where the quiescent state is linearly-stable.

0.3 Instability threshold

As a starting point for understanding the dynamics of the oscillator, we first study the linear stability of the single fixed point of Eqs. 8 and 9. This type of analysis provides insight as to how the system will respond to small perturbations. The fixed point $(x^*, y^*) = (0, 0)$ is found by setting both derivatives equal to zero and corresponds to the quiescent state of the oscillator. If we then Taylor-series expand the nonlinear term $F[x(t - \tau)]$ about $x^* = 0$ and assume a perturbation of the form $\delta y = e^{\lambda s}$, we obtain the resulting characteristic equation

$$\lambda^2 + \lambda + \epsilon + b\lambda e^{-\lambda\tau} = 0, \quad (11)$$

where $b = -\gamma d \sin(2m)$ is the effective slope of the nonlinearity in the vicinity of the fixed point. Here, λ represents the infinite number of eigenvalues whose real parts determine the stability of the solution. The quiescent state becomes linearly-unstable when $\Re[\lambda]$ becomes positive, corresponding to exponential growth away from the steady-state solution. Thus, by setting $\Re[\lambda] = 0$ and $\Im[\lambda] = \Omega$, we determine the instability threshold of the quiescent state from

$$(i\Omega)^2 + i\Omega + \epsilon + b(i\Omega)e^{-i\Omega\tau} = 0. \quad (12)$$

Separating the real terms from the imaginary terms gives the following set of equations for the instability threshold

$$-\Omega^2 + \epsilon - b\Omega \sin(\Omega\tau) = 0, \quad (13)$$

$$1 - b \cos(\Omega\tau) = 0. \quad (14)$$

Note that these equations remain unchanged for $\Omega \rightarrow -\Omega$ and, for $\epsilon > 0$, there is no solution for $\Omega = 0$. This implies that the eigenvalues cross the imaginary axis in complex conjugate pairs, which is the signature of a Hopf bifurcation. With τ and ϵ set to the values appropriate for our experimental setup, Eqs. 13 and 14 can be used to determine the values of Ω and b that give rise to a Hopf bifurcation. While the

frequency of the oscillatory motion at the onset of a Hopf bifurcation (Ω) is often of interest, here we are mainly concerned with finding b since, for a given m , it determines the gain for which a Hopf bifurcation occurs according to

$$\gamma_H = -\frac{b}{d \sin(2m)}. \quad (15)$$

For the parameter values corresponding to our experimental setup, we find that $b \approx 1$ for $m < 0$ and $b \approx -1$ for $m > 0$. One can see that, for $m = 0$, which corresponds to the operating point at the top of the interference fringe, γ_H diverges and the quiescent state of the model is linearly-stable for all values of γ , as shown by the solid lines in Fig. 4.

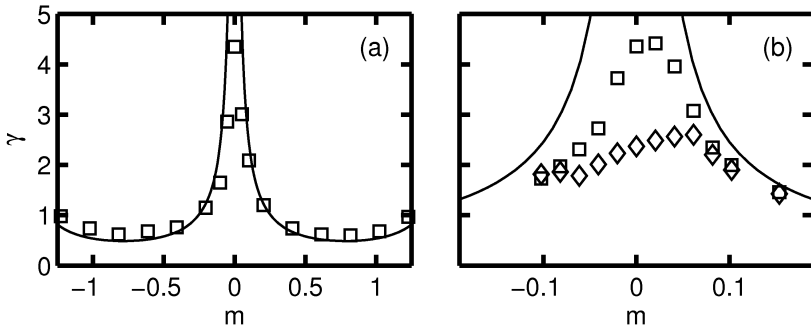


Figure 4 Observed values of γ for which the system transitions from quiescent state to oscillatory or pulsing behavior as a function of m , with γ_H superimposed (solid line). The squares in (a) and (b) indicate low experimental noise, while the diamonds in (b) indicate a higher noise level, as shown in Ref. [10]. Copyright (2010) by the American Physical Society.

Experimentally, however, we find that the situation is much more complicated than linear stability analysis predicts. In particular, as we increase γ near $m = \pm\pi/4$ we find excellent agreement between the value of γ for which the quiescent state is destabilized and γ_H , as shown in Fig. 4(a). Near $m = 0$, however, we find that the quiescent state is destabilized well before γ_H is reached, as is shown with the squares in Fig. 4(b). Interestingly, it is also near $m = 0$ where we observe broadband chaos. One can also notice a slight asymmetry in the experimentally determined instability threshold about $m = 0$, which is not predicted by linear stability analysis.

Next, we investigate the influence of noise on the instability threshold by using an erbium-doped fiber amplifier, in succession with an attenuator, to add more noise to the system while keeping the total optical power the same. We find that, by increasing the root-mean-square noise in V by a factor of 2.3 (over a bandwidth from dc to 8 GHz), we observe a substantial decrease in the instability threshold, as shown by the diamonds in Fig. 4(b). In addition, the asymmetry in the threshold is also more pronounced than in the low-noise case. Our findings indicate that the presence of experimental noise in our system, due to laser relaxation oscillations and detector dark

and shot noise, is responsible for the deviation from the linear theory. As we will show in Sec. 0.5, these features can be understood with a global (nonlinear) stability analysis of the model.

0.4

Transition to broadband chaos

To further explore the region in parameter space where broadband chaos is observed and the dynamics appear to deviate from the linear theory, we look at how the system leaves the quiescent state at the instability threshold for $m \approx 0$. A representative time series of this transient behavior is shown in Fig. 5. One can see that at around 50 ns a small pulse-like perturbation (due to noise) in V appears. At a time T later, this pulse is regenerated, but with a greater amplitude. Subsequent pulses (with a full width at half maximum of ~ 200 ps) continue to be generated each T and grow in amplitude until they begin to fold over the nonlinearity around 0.4 V and finally saturate at a maximum amplitude of about 1 V (corresponding to the input saturation voltage of the amplifier). Since noise spikes occur at random times, there can be more than one of these growing pulse trains contributing to the transient behavior (notice the spike around 280 ns, for example). In our experiments, this pulsing transient eventually gives rise to the broadband chaos we are interested in. This behavior is also verified in noise-free numerical simulations of Eqs. 8 and 9.

However, the perturbations necessary to drive the system away from the linearly-stable quiescent state do not have to originate from experimental noise. One can also apply a controlled perturbation and study its effect on the system's dynamics, both experimentally and numerically. By injecting 200-ps-long electrical pulses of varying amplitudes into the feedback loop for values of γ below the instability threshold, we find that, in general, a single input pulse will generate a train of pulses spaced in time approximately by T . For a small initial pulse amplitude, the subsequent pulse train will decay back to the quiescent state. For sufficiently large initial pulse amplitude, however, the subsequent pulse train grows and the steady-state solution is lost. For sufficiently large γ , the system transitions to the chaotic state in a quite similar manner to the transient observed when noise was providing the initial perturbation. An example of both a decaying and growing pulse train are shown in Fig. 6. We observe similar results numerically when we integrate the DDEs using a Gaussian pulse with the same width as in the experiment. The amplitudes V_{th} at which the transition between growth and decay occurs in the experiment (triangles) and simulation (stars) as a function of γ are shown in Fig. 9.

The features of these pulse trains will be exploited in the next section to understand how a small perturbation can be used to switch from the linearly-stable quiescent state to broadband chaos.

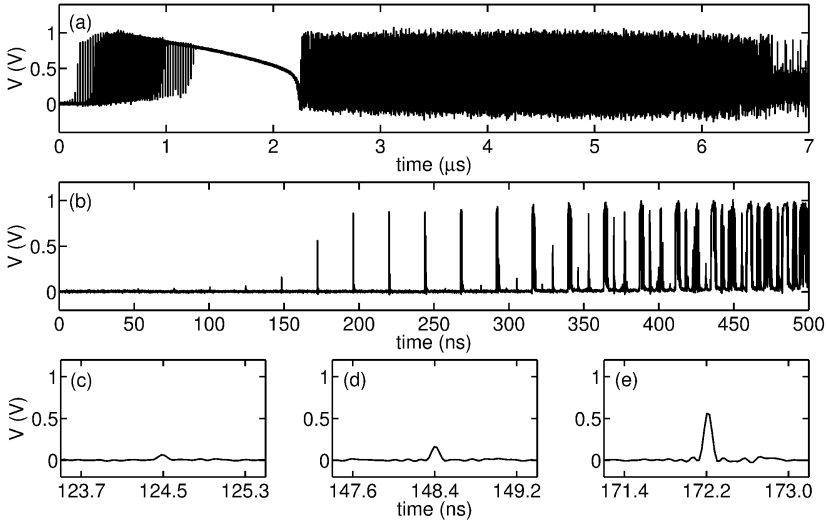


Figure 5 The transient behavior that occurs in the optoelectronic oscillator when the quiescent state first loses stability for parameter values $m = 0$ and $\gamma = 4.36$. The initial $7 \mu\text{s}$ of data (a) shows the complex breather-like behavior. A zoom in of the first 500 ns (b) shows the growing pulse trains, with three of the pulses shown in (c)-(e).

0.5 Asymptotic analysis

Our experimental observations show that, near $m = 0$, the system transitions from steady-state to non-steady-state behavior (sometimes in the form of broadband chaos) if seeded with a pulse-like perturbation of sufficient amplitude. To better understand this observation, we consider the phase portrait for Eqs. 8 and 9 with $m = 0$. The time-delay term $F[x(s - \tau)]$ vanishes when the system is in the quiescent state, leaving us with a two-dimensional ODE. Solving for the nullclines of the system under this conditions gives:

$$\dot{x} = 0 \implies y = -x, \tag{16}$$

$$\dot{y} = 0 \implies x = 0. \tag{17}$$

The intersection of the nullclines at the origin corresponds to the quiescent state of the oscillator. As ϵ is small, motion is slow in the y -direction and trajectories that start away from the stable fixed point are approximately horizontal until they reach the $y = -x$ nullcline.

Now consider what happens to the nullclines if x is perturbed with a short pulse at time $s = 0$. The feedback term $F[x(s - \tau)]$ will become nonzero for a short time in the vicinity of $s = \tau$, due to the pulse from τ earlier. This will effectively shift the

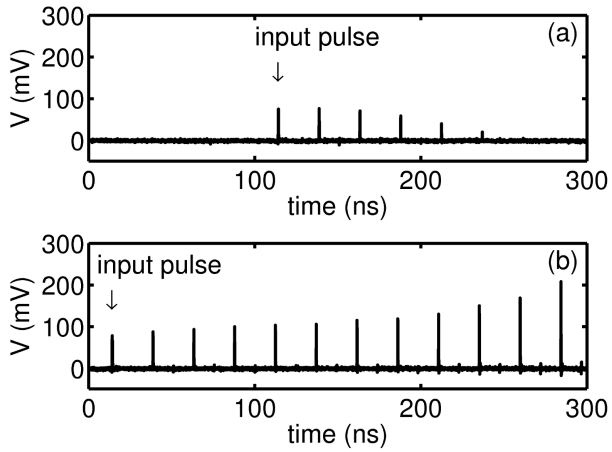


Figure 6 Two pulse trains generated by injecting pulses with amplitudes of 75.1 mV (a) and 78.7 mV (b) into the feedback loop of of the optoelectronic oscillator.

$\dot{x} = 0$ nullcline to $y = -x + \gamma \cos^2(d \tanh x_0) - \gamma$, where x_0 is the amplitude of the initial perturbation. Trajectories that start near the origin will be drawn horizontally toward the shifting nullcline in an attempt to reach the new fixed point at (x^*, y^{**}) , as shown in Fig. 7. For a sufficiently short initial pulse, the trajectories will not have enough time to move appreciably in the y -direction before the nullcline shifts back. While the motion in the y -direction is negligible, the out-and-back motion in the x -direction approximately reproduces the original pulse, but with a possibly different amplitude. As shown in Fig. 7, this pulse will be in the negative x -direction, which corresponds to the positive V -direction, regardless of the direction of the initial pulse. The pulse regeneration will continue as described with each τ as long as y does not grow appreciably.

The phase-portrait analysis presented above explains how the system operating near $m = 0$ can produce equally spaced pulses with negative amplitudes in x (positive in V) if first seeded with a pulse. The discrete nature of the trajectories in time serves as motivation to investigate a one-dimensional map of the form

$$x_{n+1} = F(x_n), \tag{18}$$

where x_n corresponds to the amplitude of a pulse at time $n\tau$, F is the nonlinear feedback term defined in Eq. 10, and the slowly changing variable y has been neglected. One should keep in mind, however, that the map given by Eq. 18 only gives approximate predictions of the dynamics of the physical system, as reducing the DDE to a map neglects all effects of the bandpass filter.

For $m = 0$, Eq. 18 can have either one or three fixed points, depending on the value of γ . The numerical solutions for the fixed points as a function of γ are shown in Fig. 8. Using standard stability analysis we find that fixed point at the origin x_{s1}^* is always

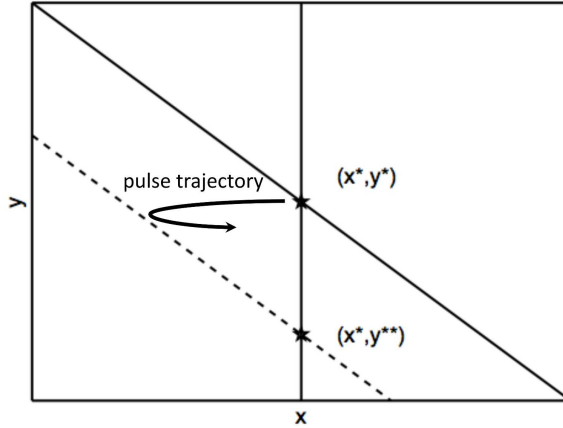


Figure 7 The nullclines with and without the presence of a pulse. The $\dot{y} = 0$ nullcline remains unchanged under the influence of a pulse, but the $\dot{x} = 0$ nullcline at $y = -x$ (solid line) is shifted to $y = -x - y^{**}$ (dashed line) when the pulse reaches its maximum amplitude. Trajectories originating near (x^*, y^*) approximately follow the shifting nullcline, but are unable to reach (x^*, y^{**}) since motion parallel to the y -axis is slow.

stable and corresponds to the quiescent state of the oscillator. When the other two fixed points exist, they are both negative. However, the fixed point with the smaller magnitude x_u^* is unstable, while the fixed point with the greater magnitude x_{s2}^* is stable. Thus, x_u^* forms a separatrix between the quiescent state x_{s1}^* and the pulsating state x_{s2}^* and can be used to give an approximate value for the critical amplitude of a pulse needed to generate a train of pulses with increasing amplitudes. The agreement between x_u^* (when converted to physical units) and the critical amplitude found in the experiment and simulation (as discussed in the previous section) is shown in Fig. 9.

Note that, for $m = 0$, the minimum perturbation size predicted by the map decreases asymptotically to zero as a function of γ . Thus, if any noise is present there exists a sufficiently large γ such that the system will leave the quiescent state near $m = 0$.

For all values of m , one can also determine the threshold gain γ_{th} required to destabilize the quiescent state for a given noise intensity $D = \sqrt{2 \langle x^2 \rangle}$, where $\langle x^2 \rangle$ is the variance of x in the stochastic analog of Eqs. 8 and 9 without feedback. First, consider determining the fixed points of the map by setting $x_{n+1} = x_n$. This gives

$$x^* = \gamma \cos^2[m + d \tanh(x^*)] - \gamma \cos^2(m), \quad (19)$$

which can be rewritten as

$$x^* = -\gamma \sin[2m + d \tanh(x^*)] \sin[d \tanh(x^*)]. \quad (20)$$

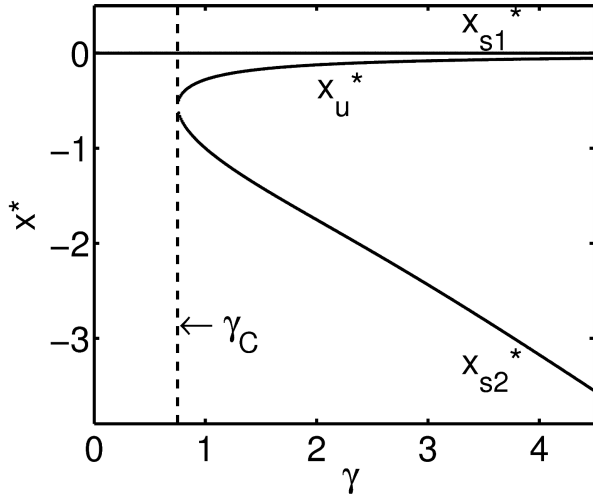


Figure 8 Fixed points of the one-dimensional map derived to approximate the system's pulsing behavior. For $\gamma > \gamma_C$ there are three fixed points (x_{s1}^* , x_u^* , and x_{s2}^*).

For the unstable fixed point x_u^* we can use the following approximation

$$x_u^* \approx -\gamma \sin(2m + dx_u^*) dx_u^*, \tag{21}$$

because $x_u^* \ll 1$. Next, we set x_u^* equal to $\langle x^2 \rangle$ to obtain

$$\gamma_{th} \approx \frac{1}{d \sin \frac{d}{\sqrt{2}} D - 2m}. \tag{22}$$

As mentioned previously, the separatrix x_u^* and pulsating state x_{s2}^* only exist in a certain region of parameter space. For a given value of m , we can determine the value of γ_C where the fixed points x_u^* and x_{s2}^* coalesce, as shown in Fig. 8. Since x_{s2}^* represents the pulsating state, the transient pulse trains that we observe are only possible for $\gamma > \gamma_C$. We determine γ_C numerically and find that there is a strong asymmetry about $m = 0$, as shown in Fig. 10, indicating the pulsing behavior is least likely around $m = \pi/4$. Also shown in Fig. 10 are γ_H (Hopf) and γ_{th} (noise threshold) for one value of the noise intensity. For $\gamma_{th} < \gamma_H$ ($\sim -\pi/4 < m \lesssim 0.1$), the quiescent state will be destabilized by a pulsing instability. For $\gamma_H < \gamma_{th}$, $\gamma \sim \gamma_H$, and small noise, the quiescent state will be destabilized by the Hopf bifurcation. Thus, we predict that the quiescent state will be unstable for $\gamma > \min[\gamma_H, \gamma_{th}]$. We see that there is qualitative agreement between $\min[\gamma_H, \gamma_{th}]$ highlighted in Fig. 10 with a thick line, and the high-noise experimental measurements (Fig. 4b).

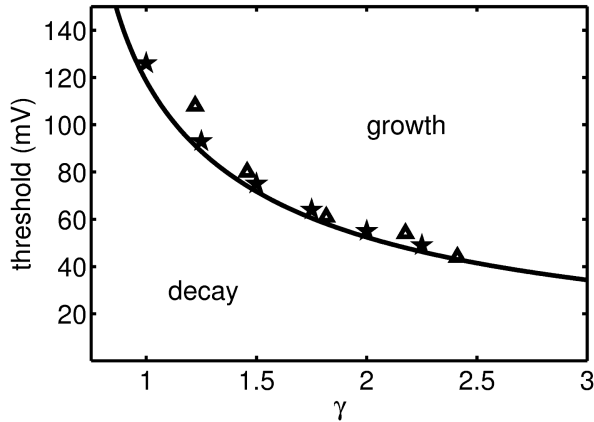


Figure 9 The pulse amplitudes V_{th} at the border between growth and decay as a function of γ in the experiment (triangles) and simulation (stars) with the unstable fixed point of the map x_u^* superimposed as a solid curve.

0.6

Summary and outlook

In summary, we have investigated the dynamics of an optoelectronic oscillator operated in a regime where the quiescent state is linearly-stable. We find experimentally and numerically that, for sufficiently high feedback gain, the system exhibits high-speed chaos with a featureless power spectrum extending beyond 8 GHz. By analyzing the experimental behavior when the system switches between these two dynamical regimes, we construct a nonlinear discrete map and find that we can predict the amplitude of a perturbation necessary to destabilize the quiescent state.

The broadband, featureless chaos generated by this device may find use in applications such as private chaos communication [15] or chaotic lidar [3], as its noise-like characteristics could improve security. In addition, the switching effect we report on might also be useful for these types of applications.

Furthermore, coexisting states are common in time-delay systems, and the existence of such states could influence these systems' stability and performance. For example, optoelectronic microwave oscillators [18], synchronized neuronal networks [19], synthetic gene networks [20], and controlled chaotic systems [21, 22] may have their noise sensitivity or stability adversely affected if a coexisting chaotic state exists and internal or external perturbations to the system are large enough that this state can be accessed.

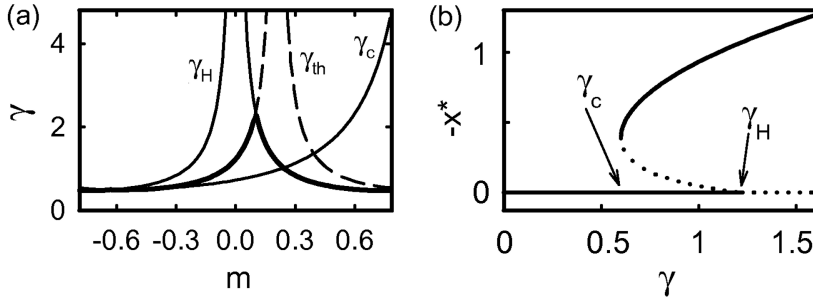


Figure 10 Instability thresholds using $D = 0.28$ in γ_{th} . Inset shows stable (solid) and unstable (dashed) fixed points vs. γ for $m = -0.2$.

0.7

Acknowledgments

Professor Eckehard Schöll has been an invaluable collaborator on this work and we have benefited greatly from his extensive knowledge of nonlinear dynamical systems. In particular, the asymptotic analysis described in Sec. 0.5 of this chapter was largely the result of his work with us during his sabbatical visit to Duke University in Spring 2008. His insights allowed us to develop a simple and intuitive picture of the transient dynamics of the optoelectronic oscillator. We are honored to have our work in this collection that celebrates his contribution to the field of nonlinear dynamics.

DJG and KEC also gratefully acknowledge the financial support of the US Office of Naval Research (N00014-07-1-0734). We thank Lauren Shareshian for helping to determine the Lyapunov exponent.

Bibliography

- 1 Pecora, L.M. and Carroll, T.M. (1990) Synchronization in chaotic systems. *Phys. Rev. Lett.*, **64**, 821–824.
- 2 Cuomo, K.M. and Oppenheim, A.V. (1993) Circuit implementation of synchronized chaos with applications to communications. *Phys. Rev. Lett.*, **71**, 65–68.
- 3 Lin, F.Y. and Liu, J.M. (2004) Chaotic lidar. *IEEE J. Sel. Top. Quantum Electron.*, **10**, 991–997.
- 4 Li, J., Fu, S., Xu, K., Wu, J., Lin, J., Tang, M., and Shum, P. (2008) Photonic ultrawideband monocycle pulse generation using a single electro-optic modulator. *Opt. Lett.*, **33**, 288–290.
- 5 Erneux, T. (2009) *Applied Delay Differential Equations*, Springer, New York, NY.
- 6 Mackey, M.C. and Glass, L. (1997) Oscillation and chaos in physiological control systems. *Science*, **197**, 287–289.
- 7 Kuang, Y. (1993) *Delay Differential Equations with Applications in Population Dynamics*, Academic Press, San Diego.
- 8 Wilson, H.R. (1999) *Spikes, decisions, and actions: the dynamical foundations of neuroscience*, Oxford University Press, Oxford, UK.
- 9 Ikeda, K. (1979) Multiple-valued stationary state and its instability of the transmitted light by a ring cavity system. *Opt. Comm.*, **30**, 257–261.
- 10 Callan, K.E., Illing, L., Gao, Z., Gauthier, D.J., and Schöll, E. (2010) Broadband chaos generated by an optoelectronic oscillator. *Phys. Rev. Lett.*, **104**, 1113 901.
- 11 Gibbs, H.M., Hopf, F.A., Kaplan, D.L., and Shoemaker, R.L. (1981) Observation of chaos in optical bistability. *Phys. Rev. Lett.*, **46**, 474–477.
- 12 Farmer, J.D. (1982) Chaotic attractors of an infinite-dimensional dynamical system. *Physica D*, **4**, 366–393.
- 13 Peil, M., Jacquot, M., Chembo, Y., Larger, L., and Erneux, T. (2009) Routes to chaos and multiple time scale dynamics in broadband bandpass nonlinear delay electro-optic oscillators. *Phys. Rev. E*, **79**, 026 208.
- 14 Kouomou, Y.C., Colet, P., Larger, L., and Gastaud, N. (2005) Chaotic breathers in delayed electro-optical systems. *Phys. Rev. Lett.*, **95**, 203 903.
- 15 Argyris, A., Syvridis, D., Larger, L., Annovazzi-Lodi, V., Colet, P., Fischer, I., García-Ojalvo, J., Mirasso, C.R., Pesquera, L., and Shore, K.A. (2005) Chaos-based communications at high bit rates using commercial fibre-optic links. *Nature*, **438**, 343–346.
- 16 Illing, L. and Gauthier, D.J. (2005) Hopf bifurcations in time-delay systems with band-limited feedback. *Physica D*, **210**, 180–202.
- 17 Udaltsov, V.S., Larger, L., Goedgebuer, J., Lee, M.W., Genin, E., and Rhodes, W.T. (2002) Bandpass chaotic dynamics of electronic oscillator operating with delayed nonlinear feedback. *IEEE*, **49**, 1006–1009.
- 18 Chembo, Y., Larger, L., and Colet, P. (2008) Nonlinear dynamics and spectral stability of optoelectronic microwave oscillators. *IEEE J. Quantum Electron.*, **44**, 858–866.
- 19 Vicente, R., Gollo, L., Mirasso, C., Fischer, I., and Pipa, G. (2008) Dynamical relaying can yield zero time lag neuronal synchrony despite long conduction delays. *P. Natl. Acad. Sci. USA*, **105**, 17 157–17 162.

- 20** Weber, W., Stelling, J., Rimann, M., Keller, B., Baba, M.D.E., Weber, C., Aubel, D., and Fussenegger, M. (2007) A synthetic time-delay circuit in mammalian cells and mice. *P. Natl. Acad. Sci. USA*, **104**, 2643–2648.
- 21** Schöll, E. and Schuster, H. (eds) (2008) *Handbook of Chaos Control, 2nd. Ed.*, Wiley-VCH, Weinheim.
- 22** Dahms, T., Hövel, P., and Schöll, E. (2008) Stabilizing continuous-wave output in semiconductor lasers by time delayed feedback. *Phys. Rev. E*, **78**, 056 213.